Quantitative T_1 and Effective Proton Density (PD*) mapping in children and adults at 7T from an MP2RAGE sequence optimised for uniform T_1-weighted (UNI) and FLuid And White matter Suppression (FLAWS) contrasts

Ayşe Sıla Dokumacı[1,2], Katy Vecchiato[2,3,4], Raphael Tomi-Tricot[1,2,5], Michael Eyre[1,2], Philippa Bridgen[1,2], Pierluigi Di Cio[1,2], Chiara Casella[2,4], Tobias C. Wood[7], Jan Sedlacik[2,8,9], Tom Wilkinson[1,2], Sharon L. Giles[1,2,10], Joseph V. Hajnal[1,2,4], Jonathan O'Muircheartaigh[2,3,4,11], Shaihan J. Malik[1,2], and David W. Carmichael[1,2]

[1]Biomedical Engineering Department, School of Biomedical Engineering and Imaging Sciences, King's College London, London, United Kingdom
[2]London Collaborative Ultra high field System (LoCUS), London, United Kingdom
[3]Department of Forensic and Neurodevelopmental Sciences, Institute of Psychiatry, Psychology and Neuroscience, King's College London, London, United Kingdom
[4]Centre for the Developing Brain, School of Biomedical Engineering and Imaging Sciences, King's College London, London, United Kingdom
[5]MR Research Collaborations, Siemens Healthcare Limited, Frimley, United Kingdom
[6]Children's Neurosciences, Evelina London Children's Hospital at Guy's and St Thomas' NHS Foundation Trust, London, UK
[7]Department of Neuroimaging, Institute of Psychiatry, Psychology and Neuroscience, King's College London, London, United Kingdom
[8]Robert Steiner MR Unit, Medical Research Council Laboratory of Medical Sciences, Hammersmith Hospital Campus, Du Cane Road, London, UK
[9]Mansfield Centre for Innovation, Imaging Sciences, Institute of Clinical Sciences, Imperial College London, Hammersmith Hospital Campus, Du Cane Road, London, UK
[10]Guy's and St Thomas' NHS Foundation Trust, London, United Kingdom
[11]MRC Centre for Neurodevelopmental Disorders, King's College London, London, United Kingdom

Corresponding Author: Ayşe Sıla Dokumacı
School of Biomedical Engineering and Imaging Sciences, King's College London
3rd Floor Lambeth Wing
St Thomas' Hospital, Westminster Bridge Road
SE1 7EH, London
E-mail: ayse.dokumaci@kcl.ac.uk
https://orcid.org/0000-0001-9035-5689

Abstract

Introduction

Quantitative MRI is important for non-invasive tissue characterisation. In previous work we developed a clinically feasible multi-contrast protocol for T_1-weighted imaging based on the MP2RAGE sequence that was optimised for both children and adults. It was demonstrated that a range of Fluid And White Matter Suppression (FLAWS) related contrasts could be produced while maintaining T_1-weighted uniform image (UNI) quality, a challenge at higher field strengths. Here we introduce an approach to use these images to calculate effective proton density (PD*) and quantitative T_1 relaxation maps especially for shorter repetition times ($TR_{MP2RAGE}$) than those typically used previously.

Methods

T_1 and PD* were estimated from the analytical equations of the MP2RAGE signal derived for partial Fourier acquisitions. The sensitivity of the fitting results was evaluated with respect to the $TR_{MP2RAGE}$ and B_1^+ effects on both excitation flip angles and inversion efficiency and compared to vendor T_1 maps which do not use B_1^+ information. Data acquired for a range of individuals (aged 10-54 years) at the shortest $TR_{MP2RAGE}$ (4000ms) were compared across white matter (WM), cortical grey matter, and deep grey matter regions.

Results

The T_1 values were insensitive to the choice of different $TR_{MP2RAGE}$. The results were similar to the vendor T_1 maps if the B_1^+ effects on the excitation flip angle and inversion efficiency were not included in the fits. T_1 values varied over development into adulthood, especially for the deep grey matter regions whereas only a very small difference was observed for WM T_1. Effective PD maps were produced which did not show a significant difference between children and adults for the age range included.

Conclusion

We produced PD* maps and improved the accuracy of T_1 maps from an MP2RAGE protocol that is optimised for UNI and FLAWS-related contrasts in a single scan at 7T by incorporating the excitation flip angle and inversion efficiency related effects of B_1^+ in the fitting. This multi-parametric protocol made it possible to acquire high resolution images (0.65mm iso) in children and adults within a clinically feasible duration (7:18 min:s). The combination of analytical equations utilizing B_1^+ maps led to T_1 fits that were consistent at different $TR_{MP2RAGE}$ values. Average WM T_1 values of adults and children were very similar (1092ms vs 1117ms) while expected reductions in T_1 with age were found for GM especially for deep GM.

Keywords: MP2RAGE, Quantitative MRI, 7T, Ultra-High Field, T_1 Mapping, PD Mapping

1 Introduction

Quantitative MRI has an important role in the measurement of tissue microstructure and its alteration as part of healthy development and ageing (Deoni, 2010; Eminian et al., 2018; Lutti et al., 2014) and in a wide range of pathology (Adler et al., 2017; McDowell et al., 2018).

Many different approaches exist for longitudinal relaxation constant (T_1) mapping (A. G. Teixeira et al., 2020; Brix et al., 1990; Christensen et al., 1974; Crawley & Henkelman, 1988; Deichmann & Haase, 1992; Deoni, 2007; Deoni et al., 2003; Frahm et al., 1986; Fram et al., 1987; Graumann et al., 1986; Gupta, 1977; Hahn, 1950; Helms et al., 2008; Henderson et al., 1999; Homer & Beevers, 1985; Leipert & Marquardt, 1976; Look & Locker, 1968, 1970; Lutti et al., 2014; Ma et al., 2023; Wright et al., 2008); however, a fast and widely used approach at 7 Tesla (T) for human brain is the Magnetization Prepared 2 Rapid Gradient Echoes (MP2RAGE) (Marques et al., 2010) sequence. The MP2RAGE sequence (Marques et al., 2010), which is an extension of the Magnetization Prepared RApid Gradient Echo (MPRAGE) sequence (Marques et al., 2010; Mugler & Brookeman, 1990; Van de Moortele et al., 2009), has been used at 7T to produce 3D structural T_1-weighted brain images and T_1 maps. This sequence acquires two Gradient Echo (GRE) images (INV1 and INV2) at two different inversion times (TI_1 and TI_2) following a non-selective adiabatic inversion pulse where the time between two consecutive inversion pulses is called $TR_{MP2RAGE}$(Marques et al., 2010). These two images are combined to form the uniform T_1-weighted image (UNI) which is insensitive to receive field (B_1^-) variability, proton density (PD), and T_2* effects (Marques et al., 2010; Van de Moortele et al., 2009). T_1 maps are typically produced using the UNI signal from look up tables (LUTs) which assume uniform B_1^+(Marques et al., 2010). Nonetheless, derived images and quantitative maps are still sensitive to transmit field (B_1^+) inhomogeneity effects (Marques et al., 2010).

Even though the MP2RAGE scan parameters can be optimised to reduce the B_1^+ effects, some residual B_1^+ bias is likely to be present in the T_1 maps (Marques & Gruetter, 2013; Van de Moortele et al., 2009). To overcome this problem, Marques et al. (Marques & Gruetter, 2013) employed the MP2RAGE sequence(Marques et al., 2010) and SA2RAGE sequence (Eggenschwiler et al., 2012) that is used to calculate B_1^+ values assuming a single T_1 value over the whole brain together (Marques & Gruetter, 2013). Two 2D look up tables relating either the T_1 value to the MP2RAGE signal intensity and the B_1^+ value or the B_1^+ value to the MP2RAGE signal intensity and the T_1 value were utilized iteratively to estimate both T_1 and B_1^+(Marques & Gruetter, 2013). The B_1^+ effect was considered only for the excitation pulses and not for the adiabatic inversion pulse (Marques & Gruetter, 2013).

A study investigating the inter-site variability compared two datasets one of which was acquired with a low B_1^+-sensitive protocol like the one by Marques and Gruetter (Marques & Gruetter, 2013) while using a parallel transmit head coil for improved B_1^+ homogeneity (Haast et al., 2021). This demonstrated that B_1^+ inhomogeneity affects both the T_1 values (Marques & Gruetter, 2013) and segmentation and cortical surface calculation (Haast et al., 2018), with differing values with and without B_1^+ inhomogeneity correction (Haast et al., 2021).

The MP2RAGE sequence can also be optimised to produce GM-dominant FLuid And White Matter Suppression (FLAWS) images (Beaumont et al., 2019, 2021; Martin et al., 2023; Massire et al., 2021; Müller et al., 2022; Tanner et al., 2012; Urushibata et al., 2019), which can be beneficial for deep GM visualisation and potentially improve lesion detection in multiple sclerosis and focal cortical dysplasia (Chen et al., 2018; Martin et al., 2023; Massire et al., 2021; Müller et al., 2022). It would be advantageous to be able to obtain T_1 maps from these protocols, but T_1 estimation is challenging due to the low grey matter (GM) signal in the bias-reduced UNI image which is used to calculate T_1 unless additional bias-reduced FLAWS-related images such as the $FLAWS_{hc}$ is used for this purpose (Beaumont et al., 2021).

A further clinically relevant quantitative value is proton density (PD) which is defined as the number of MR visible hydrogen protons in tissue (Mezer et al., 2016; Tofts, 2003). PD values have been shown to be altered in multiple sclerosis (Engström et al., 2014; Gracien et al., 2017), brain oedema in hepatic encephalopathy (Shah et al., 2008), and peritumoral oedema in malignant gliomas (Blystad et al., 2017). Quantitative PD maps can be obtained from MP2RAGE protocols; however, this has not been performed to the best of our knowledge.

A number of studies have proposed to obtain T_1 maps by adding an additional GRE block to the MP2RAGE sequence (Marques et al., 2010) named as MP3RAGE: Hung et al. (Hung et al., 2013) determined T_1 by fitting the inversion efficiency (*eff*) of the pulse as a free parameter if the pulse profile information was not available; Rioux et al. (Rioux et al., 2014) obtained T_1 and flip angle (FA) information by using three different combinations of the images acquired at different inversion times using a LUT as in Marques et al. (Marques et al., 2010); and Olsson et al. (Olsson et al., 2022) fitted T_1 and B_1^+ simultaneously by using closed-form approximations of the signal equations for small FAs while assuming an *eff* value of 0.96.

In this study, we aimed to determine if high quality T_1 and effective PD (PD*) maps could be generated from a 7T protocol with shorter than conventional repetition times ($TR_{MP2RAGE}$), previously optimised to generate UNI and FLAWS-related contrasts in a single scan (Dokumacı et al., 2023). The term effective PD has been used because the T_2* effects have not been considered(Cercignani et al., 2018; Weiskopf et al., 2013). To achieve this aim, analytical equations that account for partial Fourier acquisitions were derived and fitting was performed using the analytical equations in combination with B_1^+ maps while investigating the effects of B_1^+ both on the excitation flip angles and the inversion efficiency (*eff)*. Results using protocols with different $TR_{MP2RAGE}$ values were compared. Data from children and adults using the short TR_{MPRAGE} (=4000ms) were acquired and changes in T_1 with age were investigated.

2 Methods

2.1 Theory

The time between two consecutive inversion pulses in an MP2RAGE sequence, $TR_{MP2RAGE}$, includes two GRE blocks, the delay (TA) following the first inversion pulse until the start of the first GRE block, the delay (TB) between the two GRE blocks, and the remaining time (TC) following the second GRE block until the application of the next inversion pulse (Marques et al., 2010). Following the approach of Marques et al.(Marques et al., 2010), the MP2RAGE steady-state signal for the longitudinal magnetization and the modified signal equations accounting for the partial Fourier acquisition for the GRE blocks were derived as(Dokumaci AS, 2022):

$$m_{z,ss} = \frac{M_0\left[\left(\left((1-EA)(\cos(\alpha_1)E1)^n+(1-E1)\frac{1-(\cos(\alpha_1)E1)^n}{1-\cos(\alpha_1)E1}\right)EB+(1-EB)\right)(\cos(\alpha_2)E1)^n+(1-E1)\frac{1-(\cos(\alpha_2)E1)^n}{1-\cos(\alpha_2)E1}\right]EC+(1-EC)M_0}{1+eff(\cos(\alpha_1)\cos(\alpha_2))^n e^{-\frac{TR_{MP2RAGE}}{T_1}}} \quad (1)$$

$$GRE_{TI1} = M_0 B_1^- e^{-\frac{TE}{T_2^*}}\sin(\alpha_1)\left[\left(\frac{-eff\, m_{z,ss}}{M_0}EA+(1-EA)\right)(\cos(\alpha_1)E1)^{\frac{n}{3}}+(1-E1)\frac{1-(\cos(\alpha_1)E1)^{\frac{n}{3}}}{1-\cos(\alpha_1)E1}\right] \coloneqq M_0 k_1 \quad (2)$$

$$GRE_{TI2} = M_0 B_1^- e^{-TE/T_2^*}\sin(\alpha_2)\left[\frac{\frac{m_{z,ss}}{M_0}-(1-EC)}{EC(\cos(\alpha_2)E1)^{\frac{2n}{3}}}-(1-E1)\frac{(\cos(\alpha_2)E1)^{\frac{-2n}{3}}-1}{1-\cos(\alpha_2)E1}\right] \coloneqq M_0 k_2 \quad (3)$$

In Eqn. (1), EA = exp(-TA/T_1), EB = exp(-TB/T_1), EC = exp(-TC/T_1), and E1 = exp(-TR_{GRE}/T_1). TR_{GRE} is the time between the small flip angle excitations in the GRE blocks (n in total). The efficiency of the inversion pulse is denoted as *eff* and defined as (Marques et al., 2010) $M_{z,inv} = -eff M_z(0)$ where $M_{z,inv}$ is the inverted longitudinal magnetisation and $M_z(0)$ is the initial longitudinal magnetisation. Equations (2) and (3) account for the partial Fourier factor of 6/8 in the first phase encoding (partition) direction, acquired in the innermost k-space loop. This results in a shift of the k-space centre from the middle of the n phase encoding blocks to (n/3 + 1) in the sequence implementation.

To fit T_1 and M_0 (PD) a nonlinear least-squares solver (*lsqnonlin*) in MATLAB (R2022b, The Mathworks, Natick, Massachusetts) was used to minimise the cost function:

$\min_{\{T_1,PD\}}(f_1(seq,T_1,PD,s_1)^2 + f_2(seq,T_1,PD,s_2)^2)$ for $f_1 = s_1 - PD*k_1$ and $f_2 = s_2 - PD*k_2$ where s_1 and s_2 are the measured GRE_{TI1} and GRE_{TI2} signals, respectively with the theoretical values of $PD*k_1$ and $PD*k_2$ from Eqns. (2) and (3). The term *seq* represents the imaging parameters TR_{GRE}, TI_1, TI_2, $TR_{MP2RAGE}$, n, α_1, α_2 whose values are known. The terms k_1 and k_2 are not functions of PD but depend on T_1 and the sequence parameters.

The fitting "options" for the lsqnonlin function were MaxIterations = 100000; MaxFunctionEvaluations = 400000; FunctionTolerance = 1e-20; FiniteDifferenceStepSize = 1e-2;

and OptimalityTolerance = 1e-10. The T_1 search range was 200ms to 30000ms while for the unscaled PD 0 to 100000 was used. The initial values for T_1 and PD were 1500ms and 20000, respectively.

2.2 Different Fits for Calculating T_1

To explore the weighting of the two likely factors contributing to spatial effects (inversion efficiency (*eff*) and B_1^+ variability) different fits were performed using the nonlinear least-squares algorithm:

Fit 1 excluded B_1^+ information in the excitation flip angles (α_1 and α_2) and assumed *eff*=1 throughout the whole 3D image. **Fit 2** included B_1^+ information in the excitation flip angles (α_1 and α_2) but still assumed *eff* =1. Lastly, **Fit 3** included both the B_1^+ information and variable *eff*.

For all fits, the phase information was used to determine the polarity of the magnetization due to T_1 recovery at the first inversion time (TI_1).

The effect of $TR_{MP2RAGE}$ on the fits was investigated. In addition, T_1 maps from the vendor which are determined from a LUT without using B_1^+ information (Marques et al., 2010) were included for comparison. The function *colorbarpzn* (He, 2024) running in MATLAB was used to create the blue-white-red colormaps and colorbars.

2.3 Data Acquisition

All data was obtained under institutional ethical approval (REMAS 8700 and 18/LO/1766) and following informed consent. For all scans, a MAGNETOM Terra 7T system (Siemens Healthcare, Erlangen, Germany) using a single transmit (1Tx/32Rx) coil (Nova Medical) was employed.

The summary of scan protocols is given in Table 1. Most of the data were acquired using the protocol optimized in our previous study (Dokumacı et al., 2023) that confers the benefits of short scan time, high resolution, and high-quality FLAWS and UNI contrast options from a single scan. Firstly, data were obtained with different $TR_{MP2RAGE}$ values in a small group of 4 healthy adults (32±2 years, 1f) to assess the invariance of the T_1 estimate to the $TR_{MP2RAGE}$ (Table 1a). Secondly, data from 7 healthy children (12±2 years, 2f) and 2 more adults making it 6 adults in total (35±9 years, 1f) were obtained to determine if expected age-related T_1 changes could be observed; $TR_{MP2RAGE}$=4000ms was used for all the scans in Table 1b except for Protocol 3 which had a low sensitivity to B_1^+ with a longer $TR_{MP2RAGE}$ (Marques et al., 2010) ($TR_{MP2RAGE}$=8000ms).

To determine the effect of B_0 inclusion on the *eff* of the inversion pulse, a B_0 map (GRE sequence with 3 echoes $TE_1/TE_2/TE_3$ = 1.02ms/2.26ms/4.08ms and TR=10ms) was acquired in one subject. In addition to the B_0 map, MP2RAGE data using 2 different protocols (Protocols 2 and 3) and 2 different B_1^+ maps (sat_tfl and AFI (Yarnykh, 2007)) were obtained where sat_tfl refers to the B_1^+ method that uses a slice-selective preconditioning pulse in combination with a turbo FLASH readout (Chung et al., 2010; Fautz et al., 2008).

Table 1. TI_1/TI_2 is the time between the inversion pulse and the centre of k-space for the 1st/2nd GRE block (Marques et al., 2010). Parallel imaging was employed using GRAPPA (Griswold et al., 2002). a) Scans obtained in 4 healthy adults: a partial Fourier factor of 6/8 was used in both phase encoding directions. b) Scan parameters applied in healthy children and adults. Protocol 3 had low sensitivity to B_1^+ but a longer $TR_{MP2RAGE}$. A partial Fourier factor of 6/8 was used only in one direction (slice partial Fourier) for Protocols 2 and 3.

a)

$TR_{MP2RAGE}$ (ms)	TI_1/TI_2 (ms)	α_1/α_2 (°)	Resolution (mm^3)	Partitions	PI factor	Duration (min:s)
4000	650/2220	5/4	0.65 x 0.65 x 0.65	240	3	7:10
4500	650/2220	5/6	0.65 x 0.65 x 0.65	240	3	8:03
5000 (1)	650/2220	5/6	0.65 x 0.65 x 0.65	240	3	8:57
5000 (2)	650/2220	5/7	0.65 x 0.65 x 0.65	240	3	8:57

b)

Protocol	Subjects	$TR_{MP2RAGE}$ (ms)	TI_1/TI_2 (ms)	α_1/α_2 (°)	Resolution (mm^3)	Partitions	PI factor	Duration (min:s)
1	4 adults	4000	650/2220	5/4	0.65 x 0.65 x 0.65	240	3	7:10
2	2 adults	4000	650/2280	4/5	0.65 x 0.65 x 0.65	256	3	8:58
2	7 children	4000	650/2280	4/5	0.65 x 0.65 x 0.65	256	4	7:18
3	1 adult	8000	1000/3300	4/5	1 x 1 x 1	160	3	12:50

2.4 T_1 and PD* estimation and analysis

Data preprocessing consisted of the following steps performed in MATLAB (R2022b, The Mathworks, Natick, Massachusetts): 1) using the $FLAWS_{hco}$ images a brain mask was produced to limit the fit to brain and surrounding cerebrospinal fluid, 2) B_1^+ map processing, 3) B_1^- bias field calculation for PD* map generation, and 4) determining the inversion efficiency (*eff*) maps which are explained in detail below.

2.4.1 Producing the brain mask

$FLAWS_{hco}$ images were generated using the INV1 and INV2 images (Beaumont et al., 2021; Dokumacı et al., 2023; Tanner et al., 2012) and converted to NIfTI using the *dicm2nii* function (Li et al., 2016). A brain mask was calculated from a segmentation performed on the $FLAWS_{hco}$ image in SPM12 (Penny et al., 2007). Regions were assigned to be within the brain if they had probability of $p>0.99$ of being either white matter (WM), grey matter (GM), or cerebrospinal fluid (CSF). The resulting binary mask was edited to produce a closed mask with the application of the *imclose* and *imfill* morphological operators in MATLAB.

2.4.2 B_1^+ map processing

B_1^+ maps were smoothed using the hMRI toolbox (Tabelow et al., 2019) and co-registered and resliced using the $FLAWS_{hco}$ image (Beaumont et al., 2021; Dokumacı et al., 2023; Tanner et al., 2012) as the reference and the B_1^+ magnitude images as the source in SPM12 (Penny et al., 2007). The relative B_1^+ values for each voxel were multiplied by the nominal flip angles to define the actual flip angles subsequently used in the fitting process.

2.4.3 B_1^- related bias field calculation

Maps of the B_1^- related signal bias in the PD* fits were produced using SPM12(Penny et al., 2007) using the following parameters in the *Segment* module: extremely light regularisation (0.00001), Bias FWHM of 30 mm cutoff, and 3 different tissue types were chosen because the fits were masked.

2.4.4. Determining the inversion efficiency (eff) maps

The adiabatic inversion pulse was a hyperbolic secant (Baum et al., 1985; Silver et al., 1984) whose *eff* was determined using Bloch simulations for each spatial location for all subjects independently using the RF pulse information exported from the DICOM files in combination with the B_1^+ maps and, where available, B_0 maps.

2.5 Data Analysis in FreeSurfer

To determine the T_1 and PD* values for different brain regions, UNI images were segmented in FreeSurfer 7.3 (Fischl, 2012). For this purpose, the UNI images were masked with the same closed masks that were used in the fitting process. Masked images were denoised using the *DenoiseImage* function (Manjón et al., 2010) in Advanced Normalization Tools (ANTs)(Avants et al., 2009). A variant of the N3 Bias Correction algorithm(Sled et al., 1997, 1998), N4 Bias Correction algorithm (*N4BiasFieldCorrection* function) (Tustison et al., 2010) implemented in the ANTs (Avants et al., 2009) package was used with the default parameters (spline spacing b = 180; convergence c = [50x50x50x50, 0]). The masks were part of the inputs for both functions. Images were reoriented to standard orientation using the *fslreorient2std* function in FSL (FMRIB Software Library) (Jenkinson et al., 2012; Smith et al., 2004).

These images were segmented using the *recon-all* function (Collins et al., 1994; Dale et al., 1999; Fischl, 2004; Fischl et al., 2001, 2002; Fischl, Sereno, & Dale, 1999; Fischl, Sereno, Tootell, et al., 1999; Fischl & Dale, 2000; *Non-Uniform Intensity Correction. Http://Www.Bic.Mni.Mcgill.ca/Software/N3/Node6.Html*, n.d.; Sled et al., 1997, 1998) of FreeSurfer(Fischl, 2012) with -all (to perform all including subcortical segmentations) and -cm (to conform to the maximum resolution) options. All segmentations were checked via visual assessment by using the Subcortical Automatic Segmentation (aseg) and Automatic Cortical Parcellation (aparc) files produced by FreeSurfer overlaid on original T_1-weighted images. If the UNI image segmentation was not successful, the steps above were applied to the $FLAWS_{hco}$ images to be used as the FreeSurfer input. In one subject, parameters used for all other subjects did not result in a good segmentation and therefore were adjusted - a spline spacing of b = 100 and convergence c = [1000, 0] were used to get an improved result.

The intersection of the FreeSurfer and SPM masks were used for WM while adding another constraint to include the values with $T_1 \leq 2000$ ms to avoid contamination from CSF due to imperfect segmentation; for cortex the additional constraint was $T_1 \leq 2500$ ms. For deep GM regions, only the FreeSurfer segmentations were used because of the high constraint in the SPM

segmentation (p>0.99) leading to region of interests including very few voxels (in the extreme cases without any voxels) but, like the cortex, voxels with $T_1 \leq 2500$ ms were included in the masks. Regional T_1 mean values and standard deviations (SD) were calculated for the group of subjects who had the $TR_{MP2RAGE}$=4000ms protocols to see how the values within different brain regions change by age and to establish values in children at 7T.

3 Results

The pulse profile with the inversion efficiency simulated using the B_0 and B_1^+ maps from the scan where Protocols 2 and 3 were compared are given in Figure 1. As seen in Figure 1a-b, the inversion pulse is very efficient for a large range of B_1^+ and off-resonance values. For this slice, the inversion efficiency mean value ± standard deviation was 0.995 ± 0.023 with a minimum value of 0.477. Without the inclusion of B_0 information in the inversion efficiency calculations, the inversion efficiency for this slice was simulated as 0.995 ± 0.023 with a minimum of 0.478. Inversion efficiency over the 3D volume was calculated as 0.990 ± 0.048 and 0.990 ± 0.047 with and without the inclusion of the B_0 map, respectively.

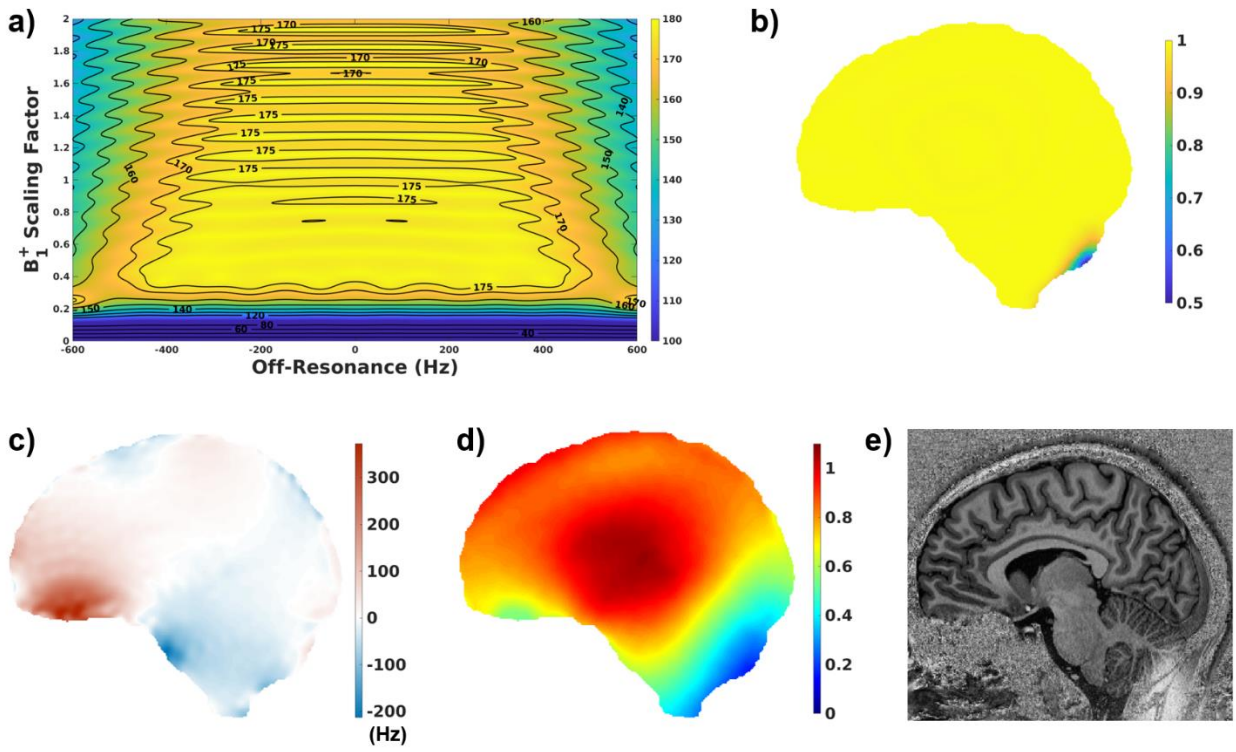

Figure 1. a) Pulse profile using a range of B_0 and B_1^+ values for this pulse which is insensitive to a large range of B_0 and B_1^+ values b) Inversion Efficiency (*eff*) map using c) B_0 map from a slice acquired in this scan and d) the corresponding B_1^+ map (sat_tfl) e) the corresponding UNI image which shows a big change at the back of the cerebellum exactly where the *eff* deviates from 1.

The differences between the vendor T_1 map which is based on a LUT that does not use B_1^+ information and the fit that uses B_1^+ information demonstrated the expected spatial effect in T_1 due to the spatial variation in the B_1^+ field (Fig. 2). Different fits (Fits 1-3) were performed to investigate the contribution of the *eff* and B_1^+ variability to these spatial effects.

Figure 3 shows the histograms of WM and cortex from the data of one adult subject using Protocol 1 for these different fits and the vendor T_1 map. Supplementary Figure 1 shows the histograms from the deep GM regions. Table 2 lists the means and standard deviations for 4 adults including this subject (Adult 1) for WM and cortex.

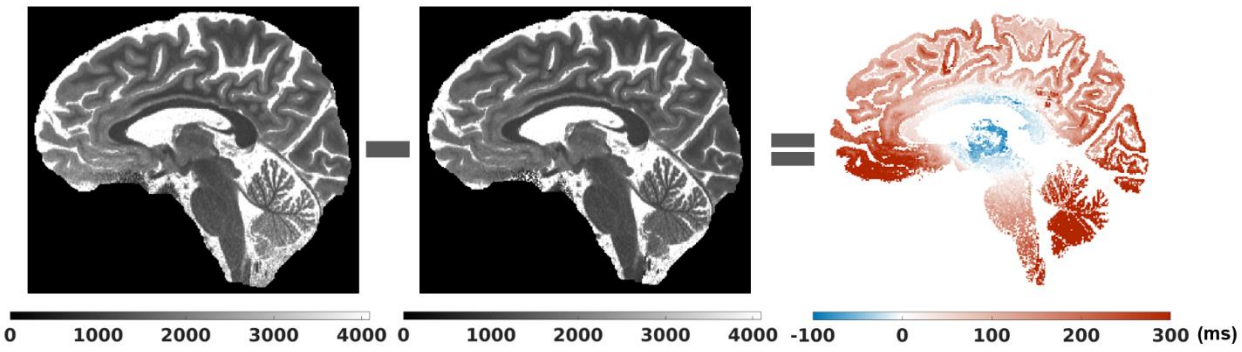

Figure 2. Vendor T_1 map (a), the fit (b), and their difference for WM and GM (c) demonstrating the spatial effect related to B_1^+ non-uniformity.

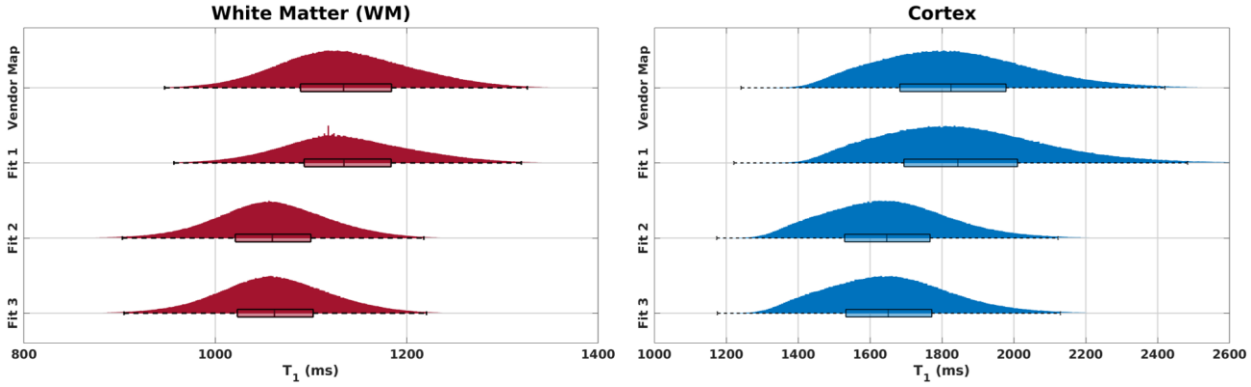

Figure 3. WM and cortex histograms for the vendor T_1 map and different fits in one adult (Adult 1). Fit 1 does not consider the B_1^+ information like the vendor map. Fit 2 considers the B_1^+ information but assumes the inversion efficiency to be uniform (*eff* = 1) for each pixel. Fit 3 uses both the B_1^+ and *eff* maps for each pixel. Fit 1 produced the closest results to those of the vendor map. The results from Fits 2 and 3 were similar because of the high inversion efficiency of the adiabatic inversion pulse (*eff* = 0.994 ± 0.028 over all subjects).

In all subjects, the mean and median values of the vendor map and Fit 1 were the closest as both ignored the B_1^+ information. For this highly efficient hyperbolic secant adiabatic inversion pulse

with an *eff* of 0.994 ± 0.028 over 13 subjects, the results from Fit 2 and Fit 3 were very similar. Supplementary Table 1 shows the T_1 results using different fits in deep GM regions where a similar trend is observed.

Table 2. Means and SDs for WM and cortex T_1 values (ms) using different fits for 4 adults (Protocol 1). As in Fig.3, the vendor map results are closest to those obtained with Fit 1 for all subjects. Likewise, Fits 2 and 3 provided very similar results due to the high inversion efficiency of the adiabatic pulse.

T_1 Value (ms)	Adult 1		Adult 2		Adult 3		Adult 4	
Mean ± SD	WM	Cortex	WM	Cortex	WM	Cortex	WM	Cortex
Vendor Map	1138 ± 72	1841 ± 217	1202 ± 81	1957 ± 229	1170 ± 67	1865 ± 227	1187 ± 77	1916 ± 218
Fit 1	1139 ± 71	1866 ± 238	1201 ± 82	2021 ± 287	1168 ± 66	1901 ± 267	1184 ± 77	1968 ± 270
Fit 2	1060 ± 62	1656 ± 178	1108 ± 67	1723 ± 184	1098 ± 54	1665 ± 191	1103 ± 60	1696 ± 177
Fit 3	1063 ± 63	1660 ± 179	1111 ± 67	1729 ± 183	1100 ± 55	1670 ± 192	1105 ± 60	1702 ± 178

To investigate the effect of $TR_{MP2RAGE}$ on T_1 fits, 4 different $TR_{MP2RAGE}$ protocols (Table 1a) were compared using the Fit 3 estimation (accounting for B_1^+ effects on both the excitation flip angles and the *eff*). In Figure 4, the T_1 means and standard deviations for different brain regions with different $TR_{MP2RAGE}$ values are shown. The standard deviation at each $TR_{MP2RAGE}$ corresponds to the physiological variation of the T_1 over the whole brain. The horizontal dotted lines correspond to the mean across $TR_{MP2RAGE}$. The mean values and the uncertainty of the average using these different protocols are given above the lines. The uncertainty of the average is very small for each brain region in all adults which indicates the high precision of the T_1 fits across $TR_{MP2RAGE}$.

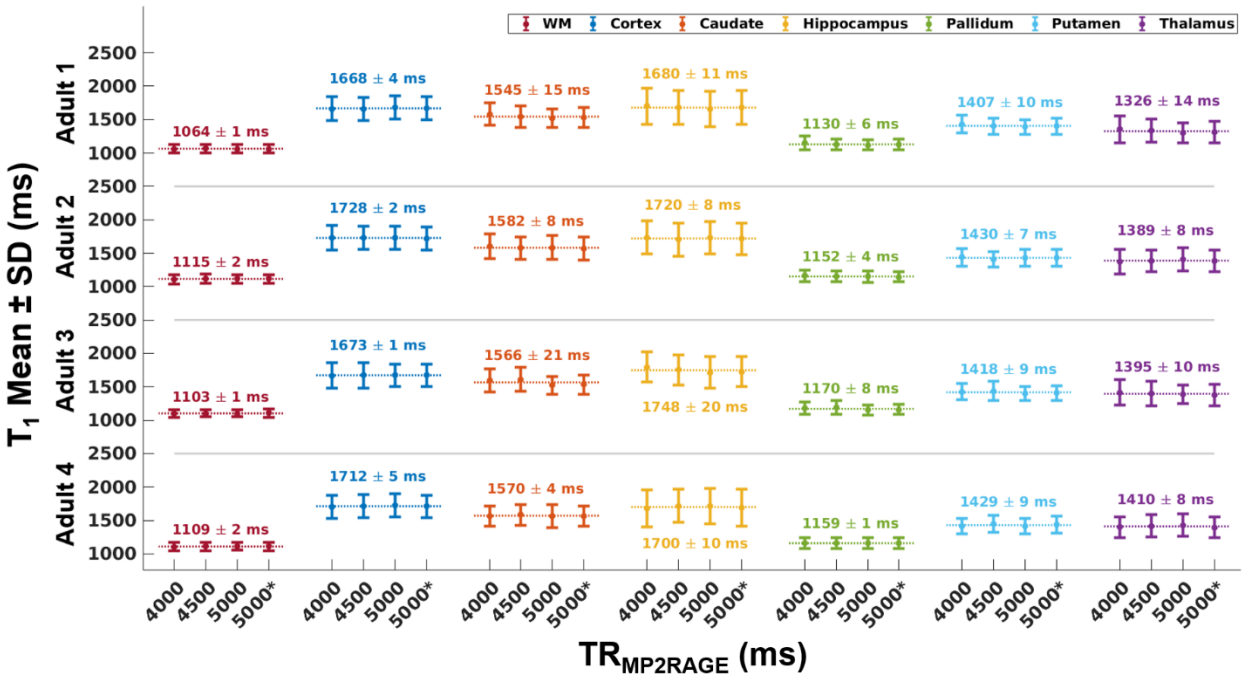

Figure 4. T_1 measurements using Fit 3 and protocols with different $TR_{MP2RAGE}$ values in 4 adults. The horizontal dotted lines correspond to the mean of the 4 measurements and the mean and uncertainty of the average is given above the line which indicates the small effect of these $TR_{MP2RAGE}$ on the fits. $TR_{MP2RAGE}$ 5000 and $TR_{MP2RAGE}$ 5000* correspond to the protocols 5000 (1) and 5000 (2) in Table 1a, respectively.

After investigating the effect of $TR_{MP2RAGE}$ on the fits, data acquired at $TR_{MP2RAGE}$=4000ms were compared in children and adults. Figure 5 shows the results from different protocols (see Table 1b for protocol summaries) for WM, cortex and deep GM structures in children and adults. The difference between children and adult T_1s was significant for GM regions especially for caudate and putamen. WM values were very similar for both populations.

The plots for PD* values in different brain regions using different protocols in children and adults are shown in Figure 6. There is not a prominent difference between children and adult PD* values. Table 3 summarizes the means and standard deviations for T_1 and PD* values of the children and adult populations.

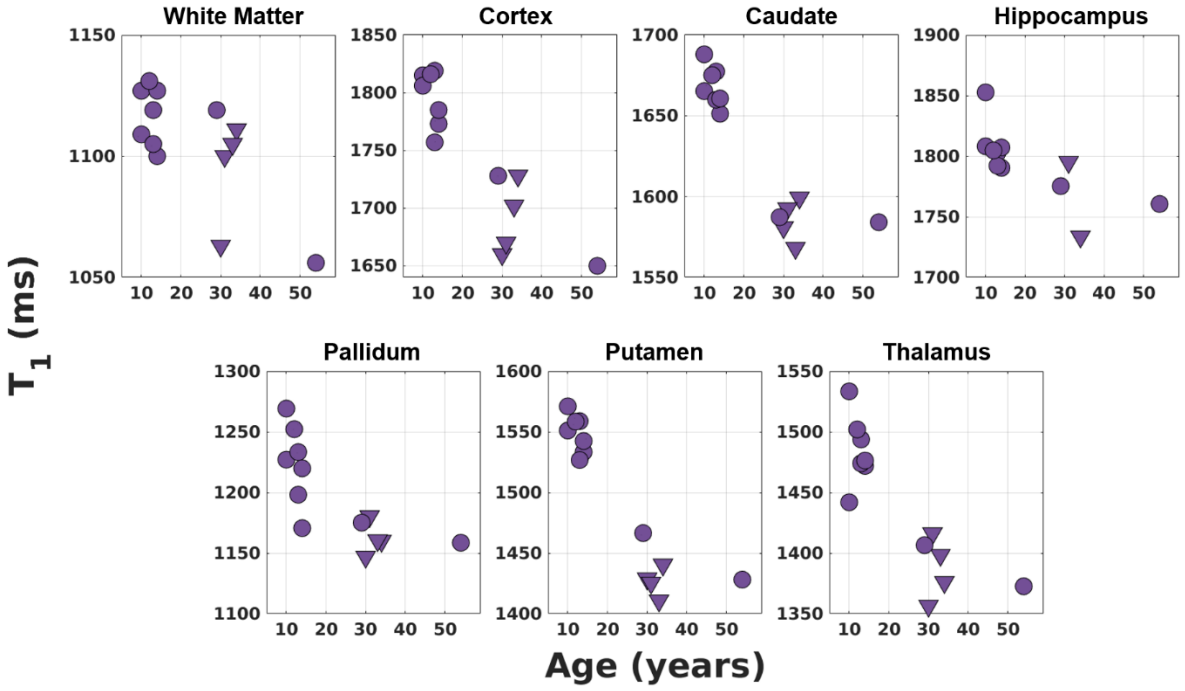

Figure 5. T_1 fits (Fit 3) using different protocols (triangles correspond to Protocol 1 and disks correspond to Protocol 2 in Table 1b) with the same $TR_{MP2RAGE}$ value (4000ms) in 7 children and 6 adults for different brain regions. The T_1 values of the children are generally higher compared to those of the adults for the GM regions especially for caudate and putamen. WM values of the children (12 ± 2 years) and adults (35 ± 9 years) are very similar.

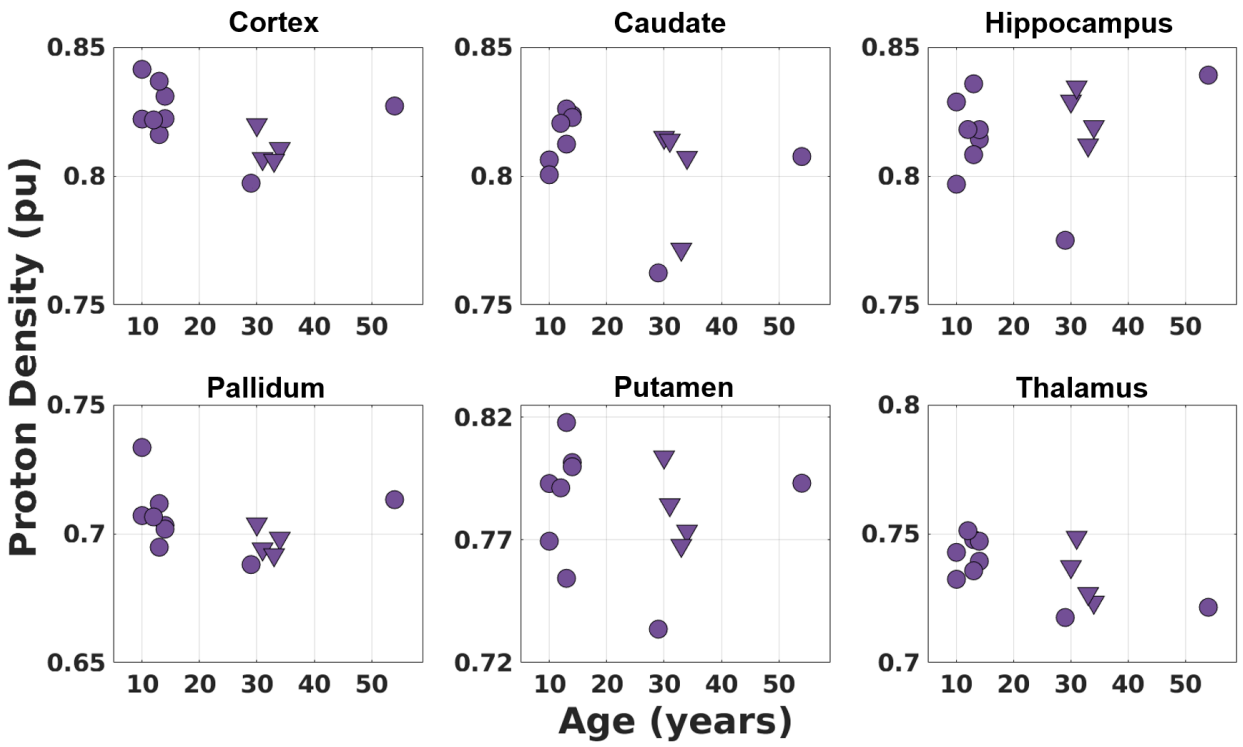

Figure 6. PD* values (Fit 3) using different protocols (triangles correspond to Protocol 1 and disks correspond to Protocol 2 in Table 1b) with the same $TR_{MP2RAGE}$ value (4000ms) in 7 children and 6 adults for different brain regions. There is not a large difference between the children and adult PD* values although thalamus PD* values suggest a very slight decrease by age. The PD* values were scaled with respect to the WM mean which was assumed to be 0.69(Weiskopf et al., 2013). No T_2* correction was made which would include a similar multiplication factor for WM and GM.

Table 3. Means and standard deviations (SD) of T_1, PD*, and B_1^+ in different brain regions of children and adults. The standard deviations reflect the physiological variation of tissue T_1 across the brain. The difference between the T_1 values of children and adults is significant for GM regions while the WM T_1 values are very close. The PD* results of children and adults are very similar as well.

	T_1 Mean ± SD (ms)				PD* Mean ± SD (pu)		$\|B_1^+\|$ Mean ± SD (pu)	
	Children Fit 3 (12 ± 2 yr)	Adults Fit 3 (35 ± 9 yr)	Children Vendor Map	Adults Vendor Map	Children Fit 3	Adults Fit 3	Children	Adults
White Matter	1117 ± 74	1092 ± 63	1221 ± 93	1180 ± 77	0.69 ± 0.04	0.69 ± 0.04	75 ± 13	74 ± 14
Cortex	1796 ± 193	1690 ± 184	2128 ± 284	1930 ± 239	0.83 ± 0.08	0.81 ± 0.07	71 ± 13	70 ± 14
Caudate	1668 ± 183	1585 ± 171	1722 ± 185	1624 ± 167	0.82 ± 0.06	0.80 ± 0.05	94 ± 6	93 ± 5
Hippocampus	1808 ± 261	1740 ± 253	2001 ± 322	1921 ± 293	0.82 ± 0.10	0.82 ± 0.10	83 ± 9	77 ± 10
Pallidum	1224 ± 96	1164 ± 96	1235 ± 101	1190 ± 105	0.71 ± 0.04	0.70 ± 0.04	97 ± 3	93 ± 3
Putamen	1549 ± 143	1433 ± 131	1649 ± 168	1523 ± 151	0.79 ± 0.05	0.78 ± 0.05	88 ± 5	85 ± 4
Thalamus	1485 ± 202	1388 ± 187	1439 ± 172	1368 ± 165	0.74 ± 0.06	0.73 ± 0.05	105 ± 5	101 ± 6

T_1 values were fitted (Fit 3) over the 3D image using 2 different B_1^+ maps for Protocol 2 ($TR_{MP2RAGE}$=4000ms) and it was also compared with Protocol 3 ($TR_{MP2RAGE}$=8000ms) which is highly insensitive to B_1^+ changes. The B_1^+ sensitivities of all protocols used in this study are given in Supplementary Figure 2. The B_1^+ maps (sat_tfl and AFI) are shown in Supplementary Figure 3 for a slice with the corresponding T_1 fits using Protocol 2.

Table 4. T_1 value comparison (Fit 3) in the same subject using different B_1^+ maps (sat_tfl and AFI) and different protocols. Protocol 3 ($TR_{MP2RAGE}$=8000ms) is less sensitive to the variations in B_1^+.

Brain Region	Protocol	B_1^+ Map	$\lvert B_1^+ \rvert$ (%)	T_1 Fit (ms)	B_1^+ Map Effect (ms)	B_1^+ Map Effect (%)	Protocol Effect (ms)	Protocol Effect (%)
White Matter	2	sat_tfl	73 ± 15	1119 ± 65	-6	-0.5	-65	-5.8
	2	AFI	74 ± 17	1125 ± 70				
	3	sat_tfl	75 ± 14	1184 ± 59				
Cortex	2	sat_tfl	68 ± 16	1728 ± 184	-14	-0.8	-24	-1.4
	2	AFI	69 ± 18	1742 ± 188				
	3	sat_tfl	68 ± 16	1752 ± 121				
Caudate	2	sat_tfl	94 ± 5	1587 ± 178	-35	-2.2	-1	-0.1
	2	AFI	98 ± 6	1622 ± 184				
	3	sat_tfl	95 ± 5	1588 ± 143				
Hippocampus	2	sat_tfl	71 ± 10	1775 ± 249	26	1.5	-54	-3
	2	AFI	67 ± 12	1749 ± 252				
	3	sat_tfl	71 ± 10	1829 ± 196				
Pallidum	2	sat_tfl	92 ± 4	1175 ± 103	-11	-0.9	-55	-4.7
	2	AFI	94 ± 7	1186 ± 106				
	3	sat_tfl	92 ± 4	1230 ± 73				
Putamen	2	sat_tfl	84 ± 4	1467 ± 140	-4	-0.3	-33	-2.2
	2	AFI	85 ± 7	1471 ± 144				
	3	sat_tfl	85 ± 4	1500 ± 107				
Thalamus	2	sat_tfl	99 ± 7	1407 ± 191	-32	-2.3	-22	-1.6
	2	AFI	102 ± 10	1439 ± 214				
	3	sat_tfl	98 ± 7	1429 ± 159				

Figure 7 demonstrates representative images and parameters maps that were produced using a single acquisition in under 7.5 minutes from a healthy child. The vendor T_1 map and the T_1 fit are displayed in the same range (0 to 4095 ms). The PD* map was scaled such that the WM mean would be equal to 0.69. No T_2^* correction was made for the PD* images. The T_2* effect is expected to be similar for WM and GM.

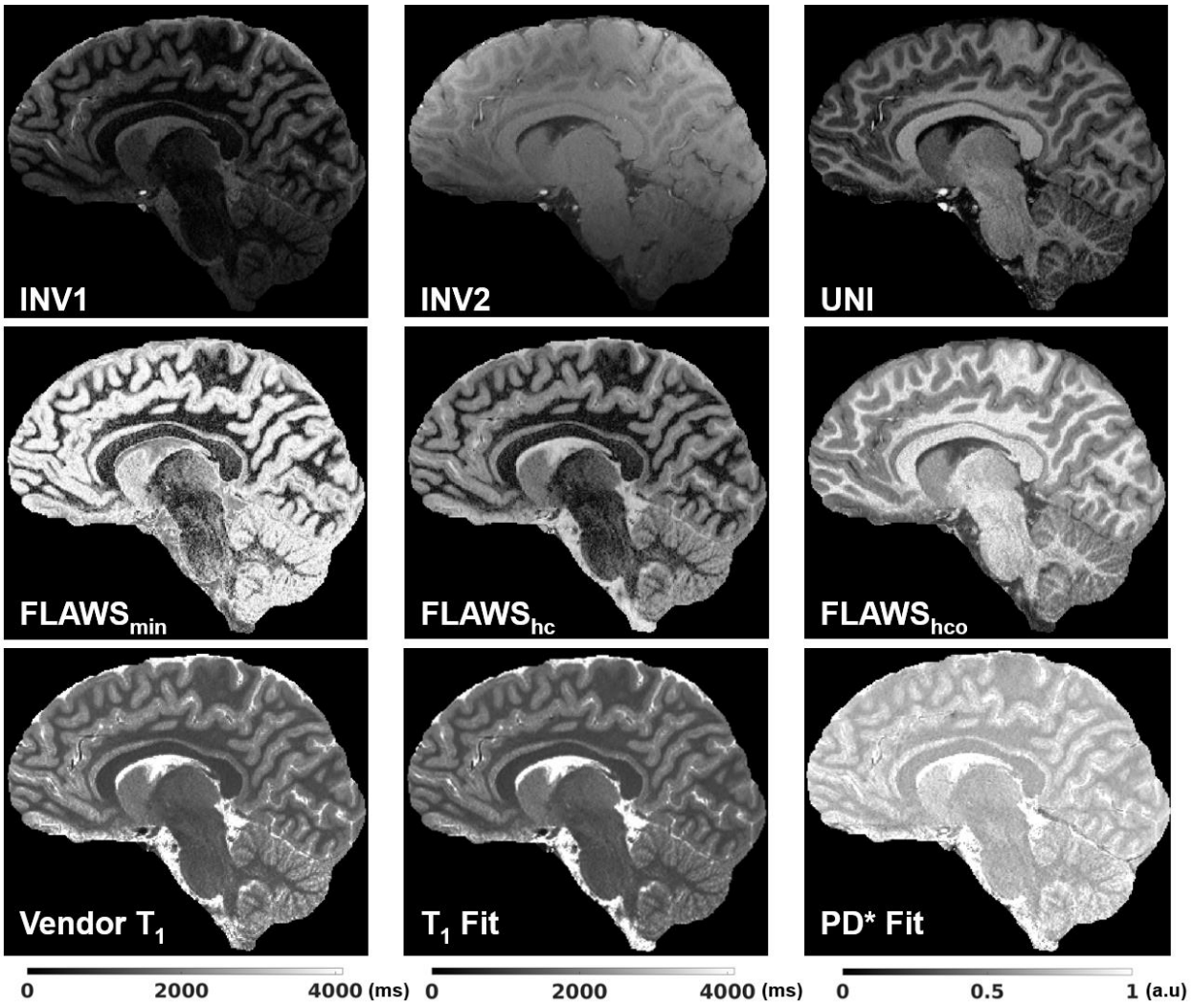

Figure 7. Different contrasts and parameter maps at 0.65 mm isotropic resolution were generated using a single MP2RAGE acquisition in 7:18 (min:s) from a healthy child. The vendor T_1 map and the T_1 fit are displayed in the same T_1 range (0 to 4095 ms). The PD* image has not been corrected for T_2* effects which would be a small factor due to the short TE (around 3 ms) and similar for WM and GM.

4 Discussion and Conclusion

In this study, we improved the accuracy of T_1 maps and derived PD* images produced from our multi-contrast protocol that is optimised for UNI and FLAWS-related contrasts in a single scan (Dokumacı et al., 2023) at 7T by including B_1^+ effects for both the excitation flip angles and the inversion pulse in the fitting. This protocol made it possible to acquire high resolution images (0.65mm iso) in children and adults thanks to its short scan duration (7:18 min:s). T_1 fitting results were consistent at different $TR_{MP2RAGE}$ values (4000 ms, 4500 ms, and 5000 ms) for different brain regions (See Fig. 4). The fits resulted in a mean adult WM T_1 value of 1092 ± 63 ms which was slightly lower than the values found in literature with the mean range of 1100-1400 ms (Marques et al., 2010; Marques & Norris, 2018; Wright et al., 2008). Mean T_1 WM value for children (12 ±

2 years) was 1117 ± 74 ms. This result being very similar to the adult T_1 is not surprising as the myelination is relatively mature after 2-3 years of age with much smaller amplitude development into adulthood (Barkovich, 2000). Cortex and deep GM regions generally had slightly lower values compared to the literature adult T_1 values (Caan et al., 2019) although they were similar and demonstrates the same pattern of lower T_1 values in deep GM regions such as the thalamus. It was observed that the GM T_1 values of children were higher than those of adults especially in deep GM regions such as caudate and putamen. This was consistent with the expected reductions in T_1 with age from literature (Cho et al., 1997; Gracien et al., 2017). Cho and colleagues (Cho et al., 1997) demonstrated at 1.5T that T_1 vs age relationship follows a quadratic curve with minimum T_1 values observed for deep GM between ages of 38-48 while the inflection in the curve does not happen before 60 years for cortex. Figure 5 shows similar trends for deep GM and cortex with a higher T_1 in the younger subjects. No significant difference was observed between the mean PD* values of children and adults (Figure 6 and Table 3). This is similar to the results from previous studies for this age range (Hagiwara et al., 2021; Saito et al., 2012). The PD* values in the thalamus (Figure 6) hints a very small decrease with age, but a larger study is required to confirm this result. Furthermore, it is possible that these small changes are related to small residual T_2*-related changes in the PD* measure, despite the relatively short TE. A study by Callaghan and colleagues(Callaghan et al., 2014) found negative correlations between effective proton density and age in the putamen, pallidum, caudate nucleus, and the red nucleus with an echo time of 8.45ms at 3T.

It was confirmed that the B_1^+ has a large effect on the T_1 values as found by Haast and colleagues (Haast et al., 2021) which necessitates future inclusion of the B_1^+ in T_1 fits. This is particularly relevant where the protocol is sensitive to B_1^+ variations at shorter $TR_{MP2RAGE}$ values which are a consequence of the requirements of short scan durations and high-resolution. The comparison of the B_1^+ corrected high-resolution images (0.65 mm isotropic) to lower-resolution images (1 mm isotropic) acquired with a low-B_1^+-sensitive protocol by Marques and Gruetter (Marques & Gruetter, 2013) revealed that by using any suitable B_1^+ map, the residual effects of B_1^+ variability on T_1 maps can be removed. The accuracy of the B_1^+ map is important as it might affect the T_1 results significantly for protocols that are more sensitive to B_1^+ variations. T_1 values fitted using two different B_1^+ mapping methods in one subject were comparable (Table 4 and Supplementary Figure 3). It could be beneficial to use protocols that are less sensitive to B_1^+ variations while satisfying the short scan duration criterion for instance by combining CS methods (Candes & Wakin, 2008; Donoho, 2006; Lustig et al., 2007; Mussard et al., 2020; Puy et al., 2012; Trotier et al., 2019, 2022; Vasanawala et al., 2010) with longer $TR_{MP2RAGE}$ values.

Quantitative results are also affected by the accuracy of the segmentations. We used an additional precaution to prevent contamination by CSF voxels by limiting the masks for T_1 values ≤ 2000 ms for WM and ≤ 2500 ms for GM. T1 restriction was found to have a negligible effect on all the values except for hippocampus which is an area more prone to segmentation errors (Supplementary Table 2).

One limitation of our study was that the B_0 map was available for only one subject. However, due to the very high inversion efficiency of this hyperbolic secant adiabatic pulse (*eff* = 0.994 ± 0.028

over all subjects), the simulated B_0 effect in the inversion efficiency using the map acquired in this subject was negligible. As seen in Figure 1, the efficiency deviates from 1 when B_1^+ is very low and it is not so related to B_0. No separate correction was made for the exponential term e^{-TE/T_2^*} but TE was very short (about 3 ms). Another limitation was that the signal equations assumed the conventional mono-exponential decay (Labadie et al., 2014; Metere et al., 2017).

In conclusion, it was possible to produce quantitative T_1 and PD* maps in children and adults at 7T in addition to the UNI and FLAWS-related contrasts from a single scan by using newly derived analytical equations required for partial Fourier acquisitions while incorporating the B_1^+ inhomogeneity effect both on the excitation flip angles and the inversion efficiency.

Acknowledgments
The authors would like to acknowledge David Leitão, Ronald Mooiweer, and Oral Ersoy Dokumaci for valuable discussions.

This research was supported by GOSHCC Sparks Grant V4419, King's Health Partners, in part by the Medical Research Council (UK) (grants MR/ K006355/1 and MR/LO11530/1) and Medical Research Council Center for Neurodevelopmental Disorders, King's College London (MR/N026063/1), and by core funding from the Wellcome EPSRC Centre for Medical Engineering at King's College London [WT203148/Z/16/Z]. J.O.M, K.V, and C.C were funded by a Sir Henry Dale Fellowship jointly by the Wellcome Trust and the Royal Society (206675/Z/17/Z). C.C was also funded by a grant from GOSHCC (VC1421). M.E was funded by Action Medical Research (GN2835) and the British Paediatric Neurology Association. This research was funded in whole, or in part, by the Wellcome Trust [WT203148/Z/16/Z and 206675/Z/17/Z] and by the National Institute for Health Research (NIHR) Biomedical Research Centre based at Guy's and St Thomas' NHS Foundation Trust and King's College London and/or the NIHR Clinical Research Facility. The views expressed are those of the author(s) and not necessarily those of the NHS, the NIHR or the Department of Health and Social Care. For the purpose of open access, the author has applied a CC BY public copyright licence to any Author Accepted Manuscript version arising from this submission.

Data Availability
The datasets that support the findings of this study are available upon request for any reasonable scientific purposes.

Competing Interests
Raphael Tomi-Tricot is an employee at Siemens Healthineers.

Author Contributions

A.S.D: Conceptualization, Methodology, Software, Validation, Formal Analysis, Investigation, Resources, Data Curation, Writing – Original Draft, Writing – Review & Editing, Visualization.
K.V: Investigation, Resources, Data Curation, Writing – Review & Editing.
R.T-T: Methodology, Software, Data Curation, Writing – Review & Editing.

M.E: Software, Investigation, Resources, Data Curation, Writing – Review & Editing.
P.B: Investigation, Resources, Data Curation, Project Administration.
P.D.C: Investigation, Resources, Data Curation.
C.C: Investigation, Resources, Data Curation, Writing – Review & Editing.
T.C.W: Methodology, Software, Validation, Writing – Review & Editing.
J.S: Software, Data Curation, Writing – Review & Editing.
T.W: Software, Data Curation.
S.L.G: Resources, Writing – Review & Editing, Project Administration.
J.V.H: Methodology, Validation, Writing – Review & Editing, Visualization.
J.O.M: Methodology, Writing – Review & Editing, Visualization, Supervision, Project Administration, Funding Acquisition.
S.J.M: Conceptualization, Methodology, Software, Validation, Formal Analysis, Writing – Review & Editing, Visualization, Supervision, Funding Acquisition.
D.W.C: Conceptualization, Methodology, Validation, Formal Analysis, Investigation, Resources, Writing – Original Draft, Writing – Review & Editing, Visualization, Supervision, Project Administration, Funding Acquisition.

References

A. G. Teixeira, R. P., Neji, R., Wood, T. C., Baburamani, A. A., Malik, S. J., & Hajnal, J. V. (2020). Controlled saturation magnetization transfer for reproducible multivendor variable flip angle T_1 and T_2 mapping. *Magnetic Resonance in Medicine*, *84*(1), 221–236. https://doi.org/10.1002/mrm.28109

Adler, S., Lorio, S., Jacques, T. S., Benova, B., Gunny, R., Cross, J. H., Baldeweg, T., & Carmichael, D. W. (2017). Towards in vivo focal cortical dysplasia phenotyping using quantitative MRI. *NeuroImage: Clinical*, *15*, 95–105. https://doi.org/10.1016/j.nicl.2017.04.017

Avants, B. B., Tustison, N., & Song, G. (2009). Advanced normalization tools (ANTS). *Insight j*, *2*(365), 1–35.

Barkovich, A. J. (2000). Concepts of myelin and myelination in neuroradiology. *AJNR. American Journal of Neuroradiology*, *21*(6), 1099–1109.

Baum, J., Tycko, R., & Pines, A. (1985). Broadband and adiabatic inversion of a two-level system by phase-modulated pulses. *Physical Review A*, *32*(6), 3435–3447. https://doi.org/10.1103/PhysRevA.32.3435

Beaumont, J., Gambarota, G., Saint-Jalmes, H., Acosta, O., Ferré, J., Raniga, P., & Fripp, J. (2021). High-resolution multi-T_1–weighted contrast and T_1 mapping with low sensitivity using the fluid and white matter suppression (FLAWS) sequence at 7T. *Magnetic Resonance in Medicine*, *85*(3), 1364–1378. https://doi.org/10.1002/mrm.28517

Beaumont, J., Saint-Jalmes, H., Acosta, O., Kober, T., Tanner, M., Ferré, J. C., Salvado, O., Fripp, J., & Gambarota, G. (2019). Multi T1-weighted contrast MRI with fluid and white matter suppression at 1.5 T. *Magnetic Resonance Imaging*, *63*, 217–225. https://doi.org/10.1016/j.mri.2019.08.010

Blystad, I., Warntjes, J. B. M., Smedby, Ö., Lundberg, P., Larsson, E.-M., & Tisell, A. (2017). Quantitative MRI for analysis of peritumoral edema in malignant gliomas. *PLOS ONE*, *12*(5), e0177135. https://doi.org/10.1371/journal.pone.0177135

Brix, G., Schad, L. R., Deimling, M., & Lorenz, W. J. (1990). Fast and precise T1 imaging using a TOMROP sequence. *Magnetic Resonance Imaging*, *8*(4), 351–356. https://doi.org/10.1016/0730-725X(90)90041-Y

Caan, M. W. A., Bazin, P., Marques, J. P., de Hollander, G., Dumoulin, S. O., & van der Zwaag, W. (2019). MP2RAGEME: T_1, T_2^*, and QSM mapping in one sequence at 7 tesla. *Human Brain Mapping*, *40*(6), 1786–1798. https://doi.org/10.1002/hbm.24490

Callaghan, M. F., Freund, P., Draganski, B., Anderson, E., Cappelletti, M., Chowdhury, R., Diedrichsen, J., FitzGerald, T. H. B., Smittenaar, P., Helms, G., Lutti, A., & Weiskopf, N. (2014). Widespread age-related differences in the human brain microstructure revealed by quantitative magnetic resonance imaging. *Neurobiology of Aging*, *35*(8), 1862–1872. https://doi.org/10.1016/j.neurobiolaging.2014.02.008

Candes, E. J., & Wakin, M. B. (2008). An Introduction To Compressive Sampling. *IEEE Signal Processing Magazine*, *25*(2), 21–30. https://doi.org/10.1109/MSP.2007.914731

Cercignani, M., Dowell, N. G., & Tofts, P. S. (2018). *Quantitative MRI of the brain: principles of physical measurement*.

Chen, X., Qian, T., Kober, T., Zhang, G., Ren, Z., Yu, T., Piao, Y., Chen, N., & Li, K. (2018). Gray-matter-specific MR imaging improves the detection of epileptogenic zones in focal cortical dysplasia: A new sequence called fluid and white matter suppression (FLAWS). *NeuroImage: Clinical*, *20*, 388–397. https://doi.org/10.1016/j.nicl.2018.08.010

Cho, S., Jones, D., Reddick, W. E., Ogg, R. J., & Steen, R. G. (1997). Establishing norms for age-related changes in proton T1 of human brain tissue in vivo. *Magnetic Resonance Imaging*, *15*(10), 1133–1143. https://doi.org/10.1016/S0730-725X(97)00202-6

Christensen, K. A., Grant, D. M., Schulman, E. M., & Walling, C. (1974). Optimal determination of relaxation times of fourier transform nuclear magnetic resonance. Determination of spin-lattice relaxation times in chemically polarized species. *The Journal of Physical Chemistry*, *78*(19), 1971–1977. https://doi.org/10.1021/j100612a022

Chung, S., Kim, D., Breton, E., & Axel, L. (2010). Rapid B_1^+ mapping using a preconditioning RF pulse with TurboFLASH readout. *Magnetic Resonance in Medicine*, *64*(2), 439–446. https://doi.org/10.1002/mrm.22423

Collins, D. L., Neelin, P., Peters, T. M., & Evans, A. C. (1994). Automatic 3D intersubject registration of MR volumetric data in standardized Talairach space. *Journal of Computer Assisted Tomography*, *18*(2), 192–205.

Crawley, A. P., & Henkelman, R. M. (1988). A comparison of one-shot and recovery methods in T1 imaging. *Magnetic Resonance in Medicine*, *7*(1), 23–34. https://doi.org/10.1002/mrm.1910070104

Dale, A. M., Fischl, B., & Sereno, M. I. (1999). Cortical Surface-Based Analysis. *NeuroImage*, *9*(2), 179–194. https://doi.org/10.1006/nimg.1998.0395

Deichmann, R., & Haase, A. (1992). Quantification of T1 values by SNAPSHOT-FLASH NMR imaging. *Journal of Magnetic Resonance (1969)*, *96*(3), 608–612. https://doi.org/10.1016/0022-2364(92)90347-A

Deoni, S. C. L. (2007). High-resolution T1 mapping of the brain at 3T with driven equilibrium single pulse observation of T1 with high-speed incorporation of RF field inhomogeneities (DESPOT1-HIFI). *Journal of Magnetic Resonance Imaging*, *26*(4), 1106–1111. https://doi.org/10.1002/jmri.21130

Deoni, S. C. L. (2010). Quantitative Relaxometry of the Brain. *Topics in Magnetic Resonance Imaging*, *21*(2), 101–113. https://doi.org/10.1097/RMR.0b013e31821e56d8

Deoni, S. C. L., Rutt, B. K., & Peters, T. M. (2003). Rapid combined T_1 and T_2 mapping using gradient recalled acquisition in the steady state. *Magnetic Resonance in Medicine*, *49*(3), 515–526. https://doi.org/10.1002/mrm.10407

Dokumaci AS, V. K. T.-T. R. B. P. E. M. W. T. C. C. S. J. W. T. G. S. H. J. M. S. O. J. C. DW. (2022). Evaluation of quantitative T1 and PD mapping at 7T from an MP2RAGE Sequence optimised to obtain UNI and FLAWS contrast images in a single scan. In *Proc. Intl. Soc. Magn. Reson. Med.* (Vol. 30, p. 1244).

Dokumacı, A. S., Aitken, F. R., Sedlacik, J., Bridgen, P., Tomi-Tricot, R., Mooiweer, R., Vecchiato, K., Wilkinson, T., Casella, C., Giles, S., Hajnal, J. V., Malik, S. J., O'Muircheartaigh, J., & Carmichael, D. W. (2023). Simultaneous Optimization of MP2RAGE T_1-weighted (UNI) and FLuid And White matter Suppression (FLAWS) brain images at 7T using Extended Phase Graph (EPG) Simulations. *Magnetic Resonance in Medicine*, *89*(3), 937–950. https://doi.org/10.1002/mrm.29479

Donoho, D. L. (2006). Compressed sensing. *IEEE Transactions on Information Theory*, *52*(4), 1289–1306. https://doi.org/10.1109/TIT.2006.871582

Eggenschwiler, F., Kober, T., Magill, A. W., Gruetter, R., & Marques, J. P. (2012). SA2RAGE: A new sequence for fast B_1^+-mapping. *Magnetic Resonance in Medicine*, *67*(6), 1609–1619. https://doi.org/10.1002/mrm.23145

Eminian, S., Hajdu, S. D., Meuli, R. A., Maeder, P., & Hagmann, P. (2018). Rapid high resolution T1 mapping as a marker of brain development: Normative ranges in key regions of interest. *PLOS ONE*, *13*(6), e0198250. https://doi.org/10.1371/journal.pone.0198250

Engström, M., Warntjes, J. B. M., Tisell, A., Landtblom, A.-M., & Lundberg, P. (2014). Multi-Parametric Representation of Voxel-Based Quantitative Magnetic Resonance Imaging. *PLoS ONE*, *9*(11), e111688. https://doi.org/10.1371/journal.pone.0111688

Fautz, H. P., Vogel, M., Gross, P., Kerr, A., & Zhu, Y. (2008). B1 mapping of coil arrays for parallel transmission. *Proceedings of the 16th Annual Meeting of ISMRM, Toronto, Canada*, *1247*.

Fischl, B. (2004). Automatically Parcellating the Human Cerebral Cortex. *Cerebral Cortex*, *14*(1), 11–22. https://doi.org/10.1093/cercor/bhg087

Fischl, B. (2012). FreeSurfer. *NeuroImage*, *62*(2), 774–781. https://doi.org/10.1016/j.neuroimage.2012.01.021

Fischl, B., & Dale, A. M. (2000). Measuring the thickness of the human cerebral cortex from magnetic resonance images. *Proceedings of the National Academy of Sciences*, *97*(20), 11050–11055. https://doi.org/10.1073/pnas.200033797

Fischl, B., Liu, A., & Dale, A. M. (2001). Automated manifold surgery: constructing geometrically accurate and topologically correct models of the human cerebral cortex. *IEEE Transactions on Medical Imaging*, *20*(1), 70–80. https://doi.org/10.1109/42.906426

Fischl, B., Salat, D. H., Busa, E., Albert, M., Dieterich, M., Haselgrove, C., van der Kouwe, A., Killiany, R., Kennedy, D., Klaveness, S., Montillo, A., Makris, N., Rosen, B., & Dale, A. M. (2002). Whole Brain Segmentation. *Neuron*, *33*(3), 341–355. https://doi.org/10.1016/S0896-6273(02)00569-X

Fischl, B., Sereno, M. I., & Dale, A. M. (1999). Cortical Surface-Based Analysis. *NeuroImage*, *9*(2), 195–207. https://doi.org/10.1006/nimg.1998.0396

Fischl, B., Sereno, M. I., Tootell, R. B., & Dale, A. M. (1999). High-resolution intersubject averaging and a coordinate system for the cortical surface. *Human Brain Mapping*, *8*(4), 272–284. https://doi.org/10.1002/(sici)1097-0193(1999)8:4<272::aid-hbm10>3.0.co;2-4

Frahm, J., Haase, A., & Matthaei, D. (1986). Rapid Three-Dimensional MR Imaging Using the FLASH Technique. *Journal of Computer Assisted Tomography*, *10*(2), 363–368. https://doi.org/10.1097/00004728-198603000-00046

Fram, E. K., Herfkens, R. J., Johnson, G. A., Glover, G. H., Karis, J. P., Shimakawa, A., Perkins, T. G., & Pelc, N. J. (1987). Rapid calculation of T1 using variable flip angle gradient refocused imaging. *Magnetic Resonance Imaging*, *5*(3), 201–208. https://doi.org/10.1016/0730-725X(87)90021-X

Gracien, R.-M., Nürnberger, L., Hok, P., Hof, S.-M., Reitz, S. C., Rüb, U., Steinmetz, H., Hilker-Roggendorf, R., Klein, J. C., Deichmann, R., & Baudrexel, S. (2017). Evaluation of brain ageing: a quantitative longitudinal MRI study over 7 years. *European Radiology*, *27*(4), 1568–1576. https://doi.org/10.1007/s00330-016-4485-1

Graumann, R., Fischer, H., & Oppelt, A. (1986). A new pulse sequence for determining T_1 and T_2 simultaneously. *Medical Physics*, *13*(5), 644–647. https://doi.org/10.1118/1.595867

Griswold, M. A., Jakob, P. M., Heidemann, R. M., Nittka, M., Jellus, V., Wang, J., Kiefer, B., & Haase, A. (2002). Generalized autocalibrating partially parallel acquisitions (GRAPPA). *Magnetic Resonance in Medicine*, *47*(6), 1202–1210. https://doi.org/10.1002/mrm.10171

Gupta, R. K. (1977). A new look at the method of variable nutation angle for the measurement of spin-lattice relaxation times using fourier transform NMR. *Journal of Magnetic Resonance (1969)*, *25*(1), 231–235. https://doi.org/10.1016/0022-2364(77)90138-X

Haast, R. A. M., Ivanov, D., & Uludağ, K. (2018). The impact of correction on <scp>MP2RAGE</scp> cortical <scp>T</scp> $_1$ and apparent cortical thickness at 7 <scp>T</scp>. *Human Brain Mapping*, *39*(6), 2412–2425. https://doi.org/10.1002/hbm.24011

Haast, R. A. M., Lau, J. C., Ivanov, D., Menon, R. S., Uludağ, K., & Khan, A. R. (2021). Effects of MP2RAGE B1+ sensitivity on inter-site T1 reproducibility and hippocampal morphometry at 7T. *NeuroImage*, *224*, 117373. https://doi.org/10.1016/j.neuroimage.2020.117373

Hagiwara, A., Fujimoto, K., Kamagata, K., Murata, S., Irie, R., Kaga, H., Someya, Y., Andica, C., Fujita, S., Kato, S., Fukunaga, I., Wada, A., Hori, M., Tamura, Y., Kawamori, R., Watada, H., & Aoki, S. (2021). Age-Related Changes in Relaxation Times, Proton Density, Myelin, and Tissue Volumes in Adult Brain Analyzed by 2-Dimensional Quantitative Synthetic Magnetic Resonance Imaging. *Investigative Radiology*, *56*(3), 163–172. https://doi.org/10.1097/RLI.0000000000000720

Hahn, E. L. (1950). Spin Echoes. *Physical Review*, *80*(4), 580–594. https://doi.org/10.1103/PhysRev.80.580

Helms, G., Dathe, H., Kallenberg, K., & Dechent, P. (2008). High-resolution maps of magnetization transfer with inherent correction for RF inhomogeneity and T_1 relaxation obtained from 3D FLASH MRI. *Magnetic Resonance in Medicine*, *60*(6), 1396–1407. https://doi.org/10.1002/mrm.21732

Henderson, E., McKinnon, G., Lee, T.-Y., & Rutt, B. K. (1999). A fast 3D Look-Locker method for volumetric T1 mapping. *Magnetic Resonance Imaging*, *17*(8), 1163–1171. https://doi.org/10.1016/S0730-725X(99)00025-9

Homer, J., & Beevers, M. S. (1985). Driven-equilibrium single-pulse observation of T1 relaxation. A reevaluation of a rapid "new" method for determining NMR spin-lattice relaxation times. *Journal of Magnetic Resonance (1969)*, *63*(2), 287–297. https://doi.org/10.1016/0022-2364(85)90318-X

Hung, W., Chen, P., Chuang, T., Chang, H., & Wu, M. (2013). High resolution volumetric T1 mapping using a novel MP3RAGE method. *International Society for Magnetic Resonance in Medicine Annual Meeting*, 2353.

Jenkinson, M., Beckmann, C. F., Behrens, T. E. J., Woolrich, M. W., & Smith, S. M. (2012). FSL. *NeuroImage*, *62*(2), 782–790. https://doi.org/10.1016/j.neuroimage.2011.09.015

Labadie, C., Lee, J., Rooney, W. D., Jarchow, S., Aubert-Frécon, M., Springer, C. S., & Möller, H. E. (2014). Myelin water mapping by spatially regularized longitudinal relaxographic imaging at high magnetic fields. *Magnetic Resonance in Medicine*, *71*(1), 375–387. https://doi.org/10.1002/mrm.24670

Leipert, T. K., & Marquardt, D. W. (1976). Statistical analysis of NMR spin-lattice relaxation times. *Journal of Magnetic Resonance (1969)*, *24*(2), 181–199. https://doi.org/10.1016/0022-2364(76)90027-5

Li, X., Morgan, P. S., Ashburner, J., Smith, J., & Rorden, C. (2016). The first step for neuroimaging data analysis: DICOM to NIfTI conversion. *Journal of Neuroscience Methods*, *264*, 47–56. https://doi.org/10.1016/j.jneumeth.2016.03.001

Look, D. C., & Locker, D. R. (1968). Nuclear Spin-Lattice Relaxation Measurements by Tone-Burst Modulation. *Physical Review Letters*, *20*(18), 987–989. https://doi.org/10.1103/PhysRevLett.20.987

Look, D. C., & Locker, D. R. (1970). Time saving in measurement of NMR and EPR relaxation times. *Review of Scientific Instruments*, *41*(2), 250–251.

Lustig, M., Donoho, D., & Pauly, J. M. (2007). Sparse MRI: The application of compressed sensing for rapid MR imaging. *Magnetic Resonance in Medicine*, *58*(6), 1182–1195. https://doi.org/10.1002/mrm.21391

Lutti, A., Dick, F., Sereno, M. I., & Weiskopf, N. (2014). Using high-resolution quantitative mapping of R1 as an index of cortical myelination. *NeuroImage*, *93*, 176–188. https://doi.org/10.1016/j.neuroimage.2013.06.005

Ma, Y.-J., Moazamian, D., Port, J. D., Edjlali, M., Pruvo, J.-P., Hacein-Bey, L., Hoggard, N., Paley, M. N. J., Menon, D. K., Bonekamp, D., Pravatà, E., Garwood, M., Danesh-Meyer, H., Condron, P., Cornfeld, D. M., Holdsworth, S. J., Du, J., & Bydder, G. M. (2023). Targeted magnetic resonance imaging (tMRI) of small changes in the T1 and spatial properties of normal or near normal appearing white and gray matter in disease of the brain using divided subtracted inversion recovery (dSIR) and divided reverse subtracted inversion recovery (drSIR) sequences. *Quantitative Imaging in Medicine and Surgery*, *13*(10), 7304–7337. https://doi.org/10.21037/qims-23-232

Manjón, J. V., Coupé, P., Martí-Bonmatí, L., Collins, D. L., & Robles, M. (2010). Adaptive non-local means denoising of MR images with spatially varying noise levels. *Journal of Magnetic Resonance Imaging*, *31*(1), 192–203. https://doi.org/10.1002/jmri.22003

Marques, J. P., & Gruetter, R. (2013). New Developments and Applications of the MP2RAGE Sequence - Focusing the Contrast and High Spatial Resolution R1 Mapping. *PLoS ONE*, *8*(7), e69294. https://doi.org/10.1371/journal.pone.0069294

Marques, J. P., Kober, T., Krueger, G., van der Zwaag, W., Van de Moortele, P.-F., & Gruetter, R. (2010). MP2RAGE, a self bias-field corrected sequence for improved segmentation and T1-mapping at high field. *NeuroImage*, *49*(2), 1271–1281. https://doi.org/10.1016/j.neuroimage.2009.10.002

Marques, J. P., & Norris, D. G. (2018). How to choose the right MR sequence for your research question at 7 T and above? *NeuroImage*, *168*, 119–140. https://doi.org/10.1016/j.neuroimage.2017.04.044

Martin, A., Emorine, T., Megdiche, I., Créange, A., Kober, T., Massire, A., & Bapst, B. (2023). Accurate Diagnosis of Cortical and Infratentorial Lesions in Multiple Sclerosis Using Accelerated Fluid and White Matter Suppression Imaging. *Investigative Radiology*, *58*(5), 337–345. https://doi.org/10.1097/RLI.0000000000000939

Massire, A., Seiler, C., Troalen, T., Girard, O. M., Lehmann, P., Brun, G., Bartoli, A., Audoin, B., Bartolomei, F., Pelletier, J., Callot, V., Kober, T., Ranjeva, J.-P., & Guye, M. (2021). T1-Based Synthetic Magnetic Resonance Contrasts Improve Multiple Sclerosis and Focal Epilepsy Imaging at 7 T. *Investigative Radiology*, *56*(2), 127–133. https://doi.org/10.1097/RLI.0000000000000718

McDowell, A. R., Shelmerdine, S. C., Carmichael, D. W., & Arthurs, O. J. (2018). High resolution isotropic diffusion imaging in post-mortem neonates: a feasibility study. *The British Journal of Radiology*, *91*(1092), 20180319. https://doi.org/10.1259/bjr.20180319

Metere, R., Kober, T., Möller, H. E., & Schäfer, A. (2017). Simultaneous Quantitative MRI Mapping of T1, T2* and Magnetic Susceptibility with Multi-Echo MP2RAGE. *PLOS ONE*, *12*(1), e0169265. https://doi.org/10.1371/journal.pone.0169265

Mezer, A., Rokem, A., Berman, S., Hastie, T., & Wandell, B. A. (2016). Evaluating quantitative proton-density-mapping methods. *Human Brain Mapping*, *37*(10), 3623–3635. https://doi.org/10.1002/hbm.23264

Mugler, J. P., & Brookeman, J. R. (1990). Three-dimensional magnetization-prepared rapid gradient-echo imaging (3D MP RAGE). *Magnetic Resonance in Medicine*, *15*(1), 152–157. https://doi.org/10.1002/mrm.1910150117

Müller, J., La Rosa, F., Beaumont, J., Tsagkas, C., Rahmanzadeh, R., Weigel, M., Bach Cuadra, M., Gambarota, G., & Granziera, C. (2022). Fluid and White Matter Suppression. *Investigative Radiology*, *57*(9), 592–600. https://doi.org/10.1097/RLI.0000000000000877

Mussard, E., Hilbert, T., Forman, C., Meuli, R., Thiran, J., & Kober, T. (2020). Accelerated MP2RAGE imaging using Cartesian phyllotaxis readout and compressed sensing reconstruction. *Magnetic Resonance in Medicine*, *84*(4), 1881–1894. https://doi.org/10.1002/mrm.28244

Non-Uniform Intensity Correction. http://www.bic.mni.mcgill.ca/software/N3/node6.html. (n.d.).

Olsson, H., Andersen, M., Kadhim, M., & Helms, G. (2022). MP3RAGE: Simultaneous mapping of T_1 and B1+ in human brain at 7T. *Magnetic Resonance in Medicine*, *87*(6), 2637–2649. https://doi.org/10.1002/mrm.29151

Penny, W., Friston, K., Ashburner, J., Kiebel, S., & Nichols, T. (2007). *Statistical Parametric Mapping: The Analysis of Functional Brain Images*. https://doi.org/10.1016/B978-0-12-372560-8.X5000-1

Puy, G., Vandergheynst, P., Gribonval, R., & Wiaux, Y. (2012). Universal and efficient compressed sensing by spread spectrum and application to realistic Fourier imaging techniques. *EURASIP Journal on Advances in Signal Processing*, *2012*(1), 6. https://doi.org/10.1186/1687-6180-2012-6

Rioux, J. A., Saranathan, M., & Rutt, B. K. (2014). Simultaneous whole-brain t1 and flip angle mapping with MP3RAGE. *Proceedings of the 22nd Annual Meeting of ISMRM, Milan, Italy*, 3216.

Saito, N., Watanabe, M., Sakai, O., & Jara, H. (2012). Human lifespan age-related changes of the brain proton density by quantitative MRI. *Proceedings of the 20th Annual Meeting of ISMRM*, 780.

Shah, N. J., Neeb, H., Kircheis, G., Engels, P., Häussinger, D., & Zilles, K. (2008). Quantitative cerebral water content mapping in hepatic encephalopathy. *NeuroImage*, *41*(3), 706–717. https://doi.org/10.1016/j.neuroimage.2008.02.057

Silver, M. S., Joseph, R. I., & Hoult, D. I. (1984). Highly selective and π pulse generation. *Journal of Magnetic Resonance (1969)*, *59*(2), 347–351. https://doi.org/10.1016/0022-2364(84)90181-1

Sled, J. G., Zijdenbos, A. P., & Evans, A. C. (1997). A Comparison of Retrospective Intensity Non-uniformity Correction Methods for MRI. *Information Processing in Medical Imaging*. https://api.semanticscholar.org/CorpusID:27760780

Sled, J. G., Zijdenbos, A. P., & Evans, A. C. (1998). A nonparametric method for automatic correction of intensity nonuniformity in MRI data. *IEEE Transactions on Medical Imaging*, *17*(1), 87–97. https://doi.org/10.1109/42.668698

Smith, S. M., Jenkinson, M., Woolrich, M. W., Beckmann, C. F., Behrens, T. E. J., Johansen-Berg, H., Bannister, P. R., De Luca, M., Drobnjak, I., Flitney, D. E., Niazy, R. K., Saunders, J., Vickers, J., Zhang, Y., De Stefano, N., Brady, J. M., & Matthews, P. M. (2004). Advances in functional and structural MR image analysis and implementation as FSL. *NeuroImage*, *23*, S208–S219. https://doi.org/10.1016/j.neuroimage.2004.07.051

Tabelow, K., Balteau, E., Ashburner, J., Callaghan, M. F., Draganski, B., Helms, G., Kherif, F., Leutritz, T., Lutti, A., Phillips, C., Reimer, E., Ruthotto, L., Seif, M., Weiskopf, N., Ziegler, G., & Mohammadi, S. (2019). hMRI – A toolbox for quantitative MRI in neuroscience and clinical research. *NeuroImage*, *194*, 191–210. https://doi.org/10.1016/j.neuroimage.2019.01.029

Tanner, M., Gambarota, G., Kober, T., Krueger, G., Erritzoe, D., Marques, J. P., & Newbould, R. (2012). Fluid and white matter suppression with the MP2RAGE sequence. *Journal of Magnetic Resonance Imaging*, *35*(5), 1063–1070. https://doi.org/10.1002/jmri.23532

Tofts, P. (2003). *Quantitative MRI of the Brain* (P. Tofts, Ed.). Wiley. https://doi.org/10.1002/0470869526

Trotier, A. J., Dilharreguy, B., Anandra, S., Corbin, N., Lefrançois, W., Ozenne, V., Miraux, S., & Ribot, E. J. (2022). The Compressed Sensing MP2RAGE as a Surrogate to the MPRAGE for Neuroimaging at 3 T. *Investigative Radiology*, *57*(6), 366–378. https://doi.org/10.1097/RLI.0000000000000849

Trotier, A. J., Rapacchi, S., Faller, T. L., Miraux, S., & Ribot, E. J. (2019). Compressed-Sensing MP2RAGE sequence: Application to the detection of brain metastases in mice at 7T. *Magnetic Resonance in Medicine*, *81*(1), 551–559. https://doi.org/10.1002/mrm.27438

Tustison, N. J., Avants, B. B., Cook, P. A., Yuanjie Zheng, Egan, A., Yushkevich, P. A., & Gee, J. C. (2010). N4ITK: Improved N3 Bias Correction. *IEEE Transactions on Medical Imaging*, *29*(6), 1310–1320. https://doi.org/10.1109/TMI.2010.2046908

Urushibata, Y., Kuribayashi, H., Fujimoto, K., Kober, T., Grinstead, J. W., Isa, T., & Okada, T. (2019). Advantages of fluid and white matter suppression (FLAWS) with MP2RAGE compared with double inversion recovery turbo spin echo (DIR-TSE) at 7T. *European Journal of Radiology*, *116*, 160–164. https://doi.org/10.1016/j.ejrad.2019.04.019

Van de Moortele, P.-F., Auerbach, E. J., Olman, C., Yacoub, E., Uğurbil, K., & Moeller, S. (2009). T1 weighted brain images at 7 Tesla unbiased for Proton Density, T2$*$ contrast and RF coil receive B1 sensitivity with simultaneous vessel visualization. *NeuroImage*, *46*(2), 432–446. https://doi.org/10.1016/j.neuroimage.2009.02.009

Vasanawala, S. S., Alley, M. T., Hargreaves, B. A., Barth, R. A., Pauly, J. M., & Lustig, M. (2010). Improved Pediatric MR Imaging with Compressed Sensing. *Radiology*, *256*(2), 607–616. https://doi.org/10.1148/radiol.10091218

Weiskopf, N., Suckling, J., Williams, G., Correia, M. M., Inkster, B., Tait, R., Ooi, C., Bullmore, E. T., & Lutti, A. (2013). Quantitative multi-parameter mapping of R1, PD*, MT, and R2* at 3T: a multi-center validation. *Frontiers in Neuroscience*, *7*. https://doi.org/10.3389/fnins.2013.00095

Wright, P. J., Mougin, O. E., Totman, J. J., Peters, A. M., Brookes, M. J., Coxon, R., Morris, P. E., Clemence, M., Francis, S. T., Bowtell, R. W., & Gowland, P. A. (2008). Water proton T1 measurements in brain tissue at 7, 3, and 1.5T using IR-EPI, IR-TSE, and MPRAGE: results and optimization. *Magnetic Resonance Materials in Physics, Biology and Medicine*, *21*(1), 121. https://doi.org/10.1007/s10334-008-0104-8

Xiaowei He (2024). Positive-zero-negative colorbar (https://www.mathworks.com/matlabcentral/fileexchange/110190-positive-zero-negative-colorbar), MATLAB Central File Exchange. Retrieved January 26, 2024. (n.d.).

Yarnykh, V. L. (2007). Actual flip-angle imaging in the pulsed steady state: A method for rapid three-dimensional mapping of the transmitted radiofrequency field. *Magnetic Resonance in Medicine*, *57*(1), 192–200. https://doi.org/10.1002/mrm.21120